Status of G2HDM with right handed neutrino coupling in the light of $b \to c\tau\nu$ anomalies

Nilakshi Das[a] **Amit Adhikary**[b] **Rupak Dutta**[c]

[a] *Indian Institute of Technology Gandhinagar, Department of Physics, Gujarat 382355, India*

[b] *Aix Marseille Univ, Université de Toulon, CNRS, CPT, IPhU, Marseille, France*

[c] *National institute of Technology Silchar 788010, Silchar, India*

E-mail: nilakshi.das@iitgn.ac.in, amit.adhikary@cpt.univ-mrs.fr, rupak@phy.nits.ac.in

Abstract: Recent experimental measurements of several observables in semileptonic B meson decays have pointed towards the possibility of new physics. The LHCb collaboration has reported a significant deviation, exceeding 3.2σ, in the combined measurement of the ratio of branching ratios $R(D) - R(D^\star)$ from the predictions of the standard model. Furthermore, other observables, such as $R_{J/\psi}$, $P_\tau^{D^\star}$, $F_L^{D^\star}$, and R_{Λ_c} in the $b \to c\ell\nu$ transition, have also exhibited noticeable deviations from the standard model predictions. Motivated by these anomalies in the $b \to c\tau\nu$ transitions, we perform a log-likelihood fit incorporating new physics coming from right-handed neutrino couplings and explored the implications of a charged Higgs boson within a generic two Higgs doublet model (G2HDM). Our comprehensive analysis, focused on the $\tau\nu$ and $b\tau\nu$ final states, was performed using the High Luminosity run of the Large Hadron Collider (HL-LHC). We demonstrate that HL-LHC has the sensitivity to exclude the remaining allowed region in G2HDM model in explaining these anomalies with charged Higgs boson coupled to right-handed neutrino.

Contents

1 Introduction

The standard model (SM) of particle physics stands as a robust and extensively tested theoretical framework that has successfully described a wide range of experimental observations. However, several phenomena and experimental measurements suggest that the SM is an incomplete description of nature. Various observations such as neutrino oscillations, the existence of dark matter, the imbalance between matter and antimatter in the universe, and various flavor anomalies in particle decays collectively highlight the necessity for further research and investigations aimed at advancing our understanding of the fundamental laws of nature.

Indications of physics beyond the Standard Model (BSM) have emerged in various aspects, notably in the field of B meson decays. Recent measurements from BaBar [1, 2], Belle [3–5], and LHCb [6–9] collaborations have unveiled significant deviations in the observables $\mathcal{R}_D$ and $\mathcal{R}_{D^\star}$ from the SM predictions. The Heavy Flavor Averaging Group (HFLAV) [10] indicates a tension of 1.6σ and 2.5σ between the measured values of $\mathcal{R}_D$ and $\mathcal{R}_{D^\star}$ and their respective SM expectations. Moreover, the combined world average exhibits a deviation of 3.31σ [10] from the SM prediction, accompanied by a correlation of -0.39 between $\mathcal{R}_D - \mathcal{R}_{D^\star}$. The LHCb collaboration has also measured the ratio of branching fractions $R_{J/\psi}$ in $B_c \to J/\psi \ell \bar{\nu}$ decays and observed a deviation of around 1.9σ from the SM prediction [11, 12]. Similarly, LHCb collaboration reported measurement of the semileptonic decay process $\Lambda_b \to \Lambda_c^+ \tau^- \bar{\nu}$, yielding a significant signal with a significance of 1.8σ [12, 13]. The measurement provides a determination of the LFUV ratio, $R_{\Lambda_c} = 0.242 \pm 0.026\,(\text{stat.}) \pm 0.071\,(\text{syst.})$. Apart from the LFUV observables, the τ polarization asymmetry, $P_\tau^{D^\star}$ [14, 15], and the longitudinal polarization fraction of $D^\star$ meson, $F_L^{D^\star}$ [16], are within 1σ of the SM expectation [12].

Several model-dependent analysis including charged scalar attempted to explain these observed anomalies. Previous studies [17–38], have shown that the charged Higgs boson ($H^\pm$) in type-III 2HDM with left-handed neutrinos can simultaneously explain the anomalies observed in R_D and $R_{D^\star}$. Our work, in this regard, is significantly different from the existing ones. We aim to explore the new physics parameter space and investigate the possibility of the charged Higgs boson with right handed neutrinos to provide a consistent explanation for the observed anomalies in various LFUV observables. To this end, we start from a model-independent fit by considering the experimental measurement of all the flavor observables, namely R_D, R_{D^*}, $P_\tau^{D^\star}$, $R_{J/\psi}$, $F_L^{D^*}$ and R_{Λ_c} in the presence of scalar new physics (NP) interaction involving right-handed neutrino. We also adopt the latest bound for the branching fraction, $\mathcal{B}(B_c \to \tau\nu) \leq 63\%$ [39] to further constrain the NP parameter space. Furthermore, we investigate the type-III Two Higgs Doublet Model (2HDM) with generic flavor structure [40, 41],

as a simple extension of the SM to explain the observed anomalies in LFUV observables.

This paper is organized as follows: The theoretical formalism, along with the relevant formulae for the LFUV observables, and the results obtained from our model-independent analyses, are presented in Section 2. In Section 3, we start with the generic 2HDM and discuss the theoretical framework along with the features of the model that are pertinent for our analysis. The collider analysis of the charged Higgs boson ($H^{\pm}$) is explored in section 4. Furthermore, we examine whether the charged Higgs with right-handed neutrino Yukawa couplings can be a possible explanation for the anomalies observed in flavor observables, in Section 5. Finally, we summarize our findings and conclude in section 6.

2 Scalar coupling sensitivity to the flavor observables

The effective Lagrangian for the $b \to c\ell\nu$ quark-level transition in the presence of scalar NP interactions involving right handed neutrino can be expressed as [42, 43]:

$$\mathcal{L}_{eff} = -\frac{4G_F}{\sqrt{2}}|V_{cb}|\left[(\bar{c}_L\gamma^\mu b_L)(\bar{l}_L\gamma_\mu\nu_L) + C^S_{LR}\bar{l}_L\,\nu_R\,\bar{c}_L\,b_R + C^S_{RR}\bar{l}_L\,\nu_R\,\bar{c}_R\,b_L\right] + \text{h.c.} \tag{2.1}$$

where G_F represents Fermi coupling constant and $|V_{cb}|$ represents the Cabibbo-Kobayashi-Maskawa (CKM) matrix element. The NP Wilson coefficients (WC), denoted as C^S_{LR} and C^S_{RR}, correspond to the scalar couplings involving right-handed neutrinos. In the presence of such NP, the flavor observables R_D, $R_{D^\star}$, $P^{D^\star}_\tau$, $F^{D\star}_L$, $R_{J/\psi}$, R_{Λ_c} and $\mathcal{B}(B_c \to \tau\bar{\nu})$, at the bottom quark mass scale m_b, can be expressed as follows [44–47]. For our analysis, we assume

the mass of the right handed neutrino to be negligibly small:

$$
\begin{aligned}
R_D &\simeq R_D^{\rm SM}\Big\{1+1.01\ |C_{RR}^S+C_{LR}^S|^2\Big\}\,,\\
R_{D^\star} &\simeq R_{D^\star}^{\rm SM}\Big\{1+0.04\ |C_{RR}^S-C_{LR}^S|^2\Big\}\,,\\
P_\tau^{D^\star} &\simeq \frac{R_{D^\star}^{\rm SM}}{R_{D^\star}}P_{\tau,{\rm SM}}^{D^\star}\Big\{1+0.07\ |C_{RR}^S-C_{LR}^S|^2\Big\}\,,\\
F_L^{D\star} &\simeq \frac{R_{D^\star}^{\rm SM}}{R_{D^\star}}F_{L,{\rm SM}}^{D\star}\Big\{1+0.08\ |C_{RR}^S-C_{LR}^S|^2\Big\}\,,\\
R_{J/\psi} &\simeq R_{J/\psi}^{\rm SM}\Big\{1+0.04\ |C_{RR}^S-C_{LR}^S|^2\Big\}\,,\\
R_{\Lambda_c} &\simeq R_{\Lambda_c}^{\rm SM}\Big\{1+0.53\ {\rm Re}[{\rm C_{RR}^S C_{LR}^{S\star}}]+0.33\ (|{\rm C_{RR}^S}|^2+|{\rm C_{LR}^S}|^2)\Big\}\,,\\
\mathcal{B}(B_c\to\tau\bar\nu) &\simeq \mathcal{B}(B_c\to\tau\bar\nu)_{\rm SM}\Big\{1+|4.35({\rm C_{RR}^S}-{\rm C_{LR}^S})|^2\Big\}
\end{aligned}
\tag{2.2}
$$

Computation of all the observables in Eq. 2.2 involves the utilization of specific form factors. For R_D, $R_{J/\psi}$ and R_{Λ_c}, we employ the lattice QCD form factors of Ref. [48], Ref. [49] and Ref. [50], respectively. To calculate the observables $R_D^\star$, $P_\tau^{D^\star}$, and $F_L^{D^\star}$, we utilize the Heavy Quark Effective Theory (HQET) form factors of Ref. [51]. All the input parameters pertinent for our analysis are presented in Appendix B. We would like to mention that the uncertainties associated with the mass parameters and decay lifetimes of the hadrons are not taken into consideration in the analysis. However, we rigorously account for the uncertainties arising from the input parameters pertaining to the form factors and the CKM matrix element $|V_{cb}|$.

To explore the NP parameter space, we perform a χ^2 fit by considering total of six measurements, namely R_D, $R_{D^\star}$, $P_\tau^{D^\star}$, $F_L^{D^\star}$, $R_{J/\psi}$, and R_{Λ_c}. We define the χ^2 fit function as follows:

$$
\chi^2 \equiv \sum_{i,j}(O^{\rm theory}-O^{\rm exp})_i\ {\rm Cov}_{ij}^{-1}\ (O^{\rm theory}-O^{\rm exp})_j\,. \tag{2.3}
$$

To perform the χ^2 fit and determine the best-fit value of the scalar coupling, we utilize the `iminuit` package [52, 53]. In this analysis, we minimize a negative log-likelihood function using a multivariate Gaussian probability density function. During the fitting procedure, we account for the correlation of -0.39 [10] between the observables R_D and $R_{D^\star}$. We assume the NP couplings to be real and varied them within the range of $(-1,+1)$. In our chi-square

analysis, we examine one NP coupling at a time and find that both couplings yield the same best-fit value. The best fit value is

$$C_{RR}^S/C_{LR}^S = -0.48 \pm 0.08.$$

The corresponding best fit value and the 1σ allowed range of each flavor observables are summarized in Table 1. It is worth mentioning that the best fit value and the 1σ allowed range of $\mathcal{B}(B_c \to \tau\nu)$ obtained with scalar NP coupling satisfies the latest bound of $\mathcal{B}(B_c \to \tau\nu) \leq 63\%$.

WC	R_D	R_D^*	$R_{J/\psi}$	R_{Λ_c}	$P_\tau^{D^*}$	$F_L^{D^*}$	$\mathcal{B}(B_c \to \tau\nu)$ (%)
Best fit	0.367	0.256	0.260	0.349	−0.500	0.468	11.79
(1σ allowed range)	(0.327, 0.407)	(0.237, 0.276)	(-0.013, 0.533)	(0.239, 0.458)	(-1.304, 0.303)	(0.392, 0.544)	(8.86, 15.25)

Table 1: *The best fit value and the corresponding* 1σ *allowed range of* R_D, R_{D^*}, $R_{J/\psi}$, R_{Λ_c}, $P_\tau^{D^*}$ *and* $F_L^{D^*}$ *with* C_{RR}^S/C_{LR}^S *NP coupling.*

In Fig. 1, we present the implications of our fit result in various 2D planes of flavor observables, namely, $R_D - R_{D^\star}$, $P_\tau^{D^\star} - F_L^{D^\star}$, $R_{J/\psi} - R_{\Lambda_c}$ planes. We show the SM results and experimental central value with black and blue $\star$ symbol, respectively. The experimental uncertainty bands at 1σ, 2σ and 3σ level are shown as elliptical contours with solid, dashed and dotted blue colored contours, respectively. The best fit value of each observables is represented by "✓" symbol. The red shaded region around it corresponds to the 1σ band, coming from the experimental and theoretical uncertainties of the flavor observables.

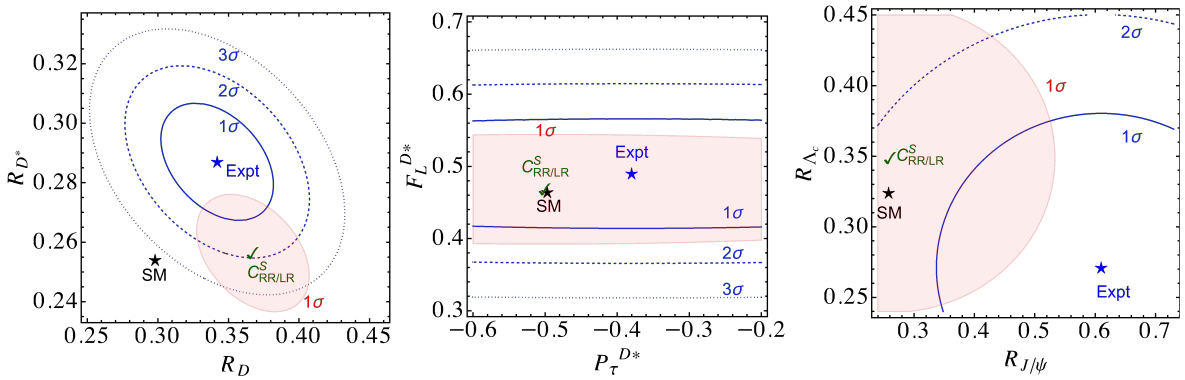

Figure 1: *The best fit value and the corresponding* 1σ *region of the flavor observables in the presence of* C_{RR}^S/C_{LR}^S *NP coupling are shown in the* $R_D - R_{D^*}$, $P_\tau^{D^\star} - F_L^{D^\star}$ *and* $R_{J/\psi} - R_{\Lambda_c}$ *planes. The blue contours represent experimental measurement at different* σ *level, whereas the SM prediction and experimental central value are denoted by black and blue star, respectively.*

As mentioned earlier in section 1, a charged Higgs in a generic 2HDM can still explain the $R_D - R_{D^\star}$ anomaly with left-handed scalar neutrino couplings. We further investigate this possibility for right-handed neutrino couplings in the subsequent sections.

3 Sensitivity of the G2HDM model

In our analysis, we examine the charged Higgs boson within the framework of a generic Two Higgs Doublet Model (G2HDM), where both Higgs doublets interact with up-type and down-type quarks. The charged Higgs ($H^\pm$) interaction can be expressed as follows [28]:

$$\mathcal{H} = \frac{\tilde{y}_{bc}\ \tilde{y}_{\tau\nu}}{m^2_{H^\pm}}(\bar{c}_R b_L)(\bar{\tau}_L \nu_{\tau R}) \tag{3.1}$$

The Yukawa couplings associated with the down-type Higgs doublets, $\tilde{y}^d_{bc}$, is constrained by the $B_s - \bar{B}_s$ mixing [41]. Thereby we concentrate on the up-type Yukawa, $\tilde{y}^u_{bc}$ interaction or the less constrained coupling C^S_{RR}. The free parameters of interest in this analysis are $\tilde{y}^u_{bc}$ (or simply denoted as $\tilde{y}_{bc}$) and $\tilde{y}_{\tau\nu}$. Our focus lies on the $b \to c\tau\bar{\nu}$ transition, mediated by a charged Higgs. This transition can be described by an effective Hamiltonian, which can be parameterized as follows:

$$\mathcal{H}_{\text{eff}} = 2\sqrt{2}G_F V_{cb}[(\bar{c}_L\gamma_\mu b_L)(\bar{\tau}_L\gamma^\mu \nu_{\tau L}) + C^S_{RR}(\bar{c}_R b_L)(\bar{\tau}_L \nu_{\tau R})]. \tag{3.2}$$

In this context, the scalar coupling C^S_{RR} is defined at the scale of the charged Higgs mass ($m_{H^\pm}$) as follows:

$$C^S_{RR} = \frac{\tilde{y}_{bc}\ \tilde{y}_{\tau\nu}}{2\sqrt{2}G_F V_{cb} m^2_{H^\pm}}. \tag{3.3}$$

It is important to note that the value of C^S_{RR} used in the definition of flavor observables in Eq. 2.2 is defined at the scale of the bottom quark mass (m_b). Hence, we employ the renormalization group equation (RGE) running of C^S_{RR} from the charged Higgs mass scale ($m_{H^\pm}$) to the m_b scale, following the prescribed procedure outlined in [54].

We do a collider analysis focusing on the final states $\tau\nu$ and $b\tau\nu$ in the following sections. These results will subsequently be utilized to impose constraints on the Yukawa coupling under investigation.

4 Collider analysis

To address the simultaneous explanation of the $R_D - R_{D^\star}$ anomaly, the collider prospects of a charged Higgs boson in the $\tau\nu$ final state have been examined in Ref. [35, 36]. It has been demonstrated that the inclusion of an extra b-tagged jet can further enhance the search potential [36]. Previous searches at the LHC have placed constraints on the decay of a charged Higgs boson into a hadronic τ (τ_h), primarily through $W' \to \tau\nu$ searches [55, 56]. However, these searches still allow for a low-mass range of the charged Higgs boson, with $m_{H^\pm} \leq 400$ GeV [36].

In this study, we analyze both the $pp \to H^\pm \to \tau_h\nu$ (b-veto category) and $pp \to bH^\pm \to b\tau_h\nu$ (b-tag category) processes, at the HL-LHC. Signal and background events are generated at the leading order (LO) using `MadGraph5_aMC@NLO` [57]. During the event generation process, specific generation-level cuts are applied, and their details can be found in Appendix A (refer to Table 8). `NNPDF2.3NLO` parton distribution function (PDF) set [58] is used. Subsequent showering and hadronization of the generated events are carried out using `Pythia8` [59] with the `A14` tune [60]. The reconstruction of jets is performed within the `FastJet` framework [61], utilizing the anti-kT clustering algorithm [62] with a jet parameter $R = 0.4$ and a transverse momentum threshold of $p_T > 15$ GeV. To simulate the detector response, we employ `Delphes-3.5.0` [63] with the default HL-LHC ATLAS analysis card.

The primary source of irreducible background contribution in both the b-veto and b-tag category arises from the $W \to \tau\nu$ process (see Fig. 2 (right)). To generate this background, we incorporate two additional jets using the MLM merging scheme [64]. The extra jet can consist of gluon, light quarks, c-quark, and b-quark. The next dominant background contamination originates from fake-τ_h events and Drell-Yan (DY) production. We generate the $jj\nu\nu$ process, where the light jets, denoted as j, can mimic a hadronic τ (τ_h). We refer to this background as the "Misid. τ_h" background. To improve upon event statistics, we generate the DY process ($pp \to \tau\tau$) separately in different $m_{\tau\tau}$ mass regions. These regions are subsequently combined with appropriate cross-section factors. For the di-boson (VV) background, we simulate the WW, WZ, and ZZ processes separately. The DY+jets and VV+jets backgrounds are generated with two extra jets using the MLM merging scheme [64]. A notable contribution to the background arises from top pair ($t\bar{t}$) production due to its large production cross-section. We generate this background in three categories: fully hadronic $t\bar{t}$, semi-leptonic $t\bar{t}$ (where one W boson decays hadronically and the other decays leptonically), and fully leptonic $t\bar{t}$ (where both W bosons decay leptonically). Lastly, we simulate the single-top background by merging it with one additional jet.

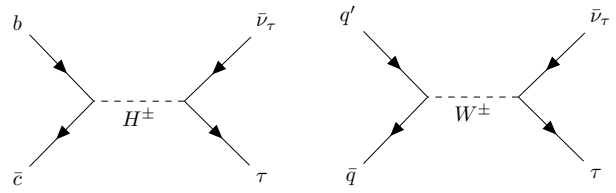

Figure 2: *Feynman diagrams for the signal process, $bc \to H^\pm \to \tau\nu$ (left) and the dominant irreducible background, $pp \to W^\pm \to \tau\nu$ (right), at leading order.*

4.1 The $\tau_h\nu$ channel

The objective of this section is to investigate the reach of the HL-LHC in constraining low-mass charged Higgs bosons within the general 2HDM model. We perform an optimized cut-based analysis by varying the charged Higgs mass, considering the following benchmark points: $m_{H^\pm} = 180,\ 200,\ 250,\ 300,\ 350$ and 400 GeV.

Our analysis criteria are as follows: We select events that contain exactly one τ-tagged jet with a transverse momentum (p_T) greater than 30 GeV and a pseudorapidity ($|\eta|$) within the range of $|\eta| < 4.0$. Leptons (e, μ) with p_T exceeding 20 GeV and $|\eta|$ within $|\eta| < 4.0$ are vetoed. Events are required to have zero b-tagged jets with p_T greater than 30 GeV and $|\eta|$ within $|\eta| < 4.0$. Furthermore, the total number of light jets in an event should not exceed two. This specific requirement significantly reduces the backgrounds from hadronic and semi-leptonic top pair ($t\bar{t}$) production. After applying the generation level cuts used for signal and background generation (see Appendix A), we proceed with a similar analysis as performed by CMS [55] with regards to the basic selection cuts. We impose a cut on the azimuthal angle separation between the τ-tagged jet and the missing transverse momentum, requiring $\Delta\phi(p_{T,\tau_h}, \not{p}_T) \geq 2.4$. In signal processes, the hadronic τ and neutrino are produced nearly back-to-back. Consequently, the missing transverse momentum and p_{T,τ_h} should exhibit small differences, arising from the dilution of neutrino momentum resulting from the τ_h decay. Therefore, the ratio of p_{T,τ_h} to $\not{p}_T$ is constrained within the range $0.7 \leq p_{T,\tau_h}/\not{p}_T \leq 1.3$. The normalized kinematic distributions of $\Delta\phi(p_{T,\tau_h}, \not{p}_T)$ and $p_{T,\tau_h}/\not{p}_T$ are presented in Fig. 3 for $m_{H^\pm} = 180$ and 400 GeV, including all relevant backgrounds.

Following the selection cuts, we perform a cut-based analysis by optimizing the cuts on three observables: transverse momentum of the τ-tagged jet (p_{T,τ_h}), transverse mass (m_T), and missing transverse energy ($\not{E}_T$). The objective is to maximize the signal significance, defined as $\sigma_s = S/\sqrt{B}$, where S and B represent the signal and background yields at a given integrated luminosity. Table 2 summarizes the trigger, basic selection, and optimized cuts for each observable. It is observed that the optimized cuts become stricter as the charged Higgs mass increases. This is consistent with the trend observed in Fig. 3, where the signal

Cuts applied	
Trigger cuts	Basic selection cuts
$N_{\tau_h} = 1,\ N_\ell = 0$ b-veto, $N_{\text{b-jets}} = 0$ $N_j \leq 2$	$\Delta\phi(p_{T,\tau_h}, \not{p}_T) \geq 2.4$ $0.7 \leq p_{T,\tau_h}/\not{p}_T \leq 1.3$
Optimised cuts	
$p_{T,\tau_h} \geq [50, 50, 70, 80, 90, 110]$ GeV $m_T \geq [100, 110, 150, 170, 200, 220]$ GeV $\not{E}_T \geq [50, 50, 60, 80, 90, 100]$ GeV	for $m_{H^\pm} = [180, 200, 250, 300, 350, 400]$ GeV

Table 2: *Cuts imposed on the cut-based analysis in* $pp \to H^\pm \to \tau_h\nu$ *channel.*

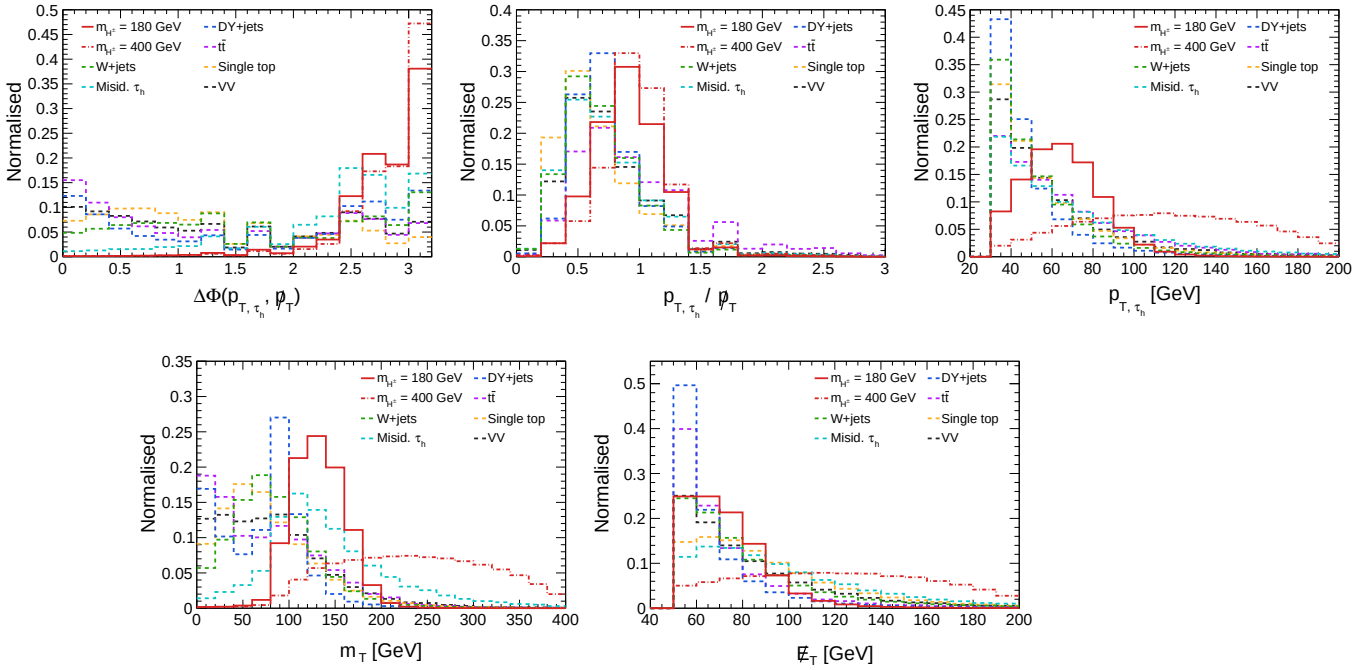

Figure 3: *The normalised kinematic distributions of* $\Delta\phi(p_{T,\tau_h}, \not{p}_T)$, $p_{T,\tau_h}/\not{p}_T$, p_{T,τ_h}, m_T *and* $\not{E}_T$ *for charged Higgs masses of* $m_{H^\pm} = 180$ *and 400 GeV with backgrounds, for the b-veto category. The distributions are shown after the basic trigger and generation level cuts.*

kinematic distributions become flatter with increasing $m_{H^\pm}$, and a stronger cut enhances the separation between the signal and background. To quantify the impact of each cuts, we provide a cut-flow table in Table 3 for $m_{H^\pm} = 180$ and 400 GeV. This table illustrates the number of background events at the HL-LHC and signal efficiency remaining after each stage of the analysis, allowing for a clear understanding of the signal and background contributions at each step.

Cut flow	Signal Efficiency, ϵ ($\times 10^{-2}$)	Background rates at $\sqrt{s} = 14$ TeV with $\mathcal{L} = 3$ ab^{-1}							
		W+jets	Misid. τ_h	DY+jets	$t\bar{t}$ had	$t\bar{t}$ semi-lep	$t\bar{t}$ lep	VV+jets	Single t
		($\times 10^7$)			($\times 10^5$)			($\times 10^6$)	
$m_{H^\pm} = 180$ GeV									
Trigger+Gen	19.9	14.9	2.0	4.3	10.1	44.5	7.8	9.7	3.1
$N_j \leq 2$	19.8	13.6	1.7	3.9	2.0	22.4	6.3	7.2	2.4
$\Delta\phi(p_{T,\tau_h}, \not{p}_T)$	17.8	4.7	1.1	1.7	0.6	3.2	2.2	2.1	0.5
$p_{T,\tau_h}/\not{p}_T$	13.0	2.8	0.44	0.86	0.25	1.3	0.8	0.9	0.2
p_{T,τ_h}	11.5	2.2	0.41	0.43	0.20	1.1	0.75	0.77	0.16
m_T	10.7	2.1	0.41	0.40	0.19	1.1	0.72	0.75	0.16
$\not{E}_T$	10.7	2.1	0.41	0.40	0.19	1.1	0.72	0.75	0.16
$m_{H^\pm} = 400$ GeV									
Trigger+Gen	28.0	14.9	2.0	4.3	10.1	44.5	7.8	9.7	3.1
$N_j \leq 2$	27.7	13.6	1.7	3.9	2.0	22.4	6.3	7.2	2.4
$\Delta\phi(p_{T,\tau_h}, \not{p}_T)$	25.5	4.7	1.1	1.7	0.6	3.2	2.2	2.1	0.5
$p_{T,\tau_h}/\not{p}_T$	20.0	2.8	0.44	0.86	0.25	1.3	0.8	0.9	0.2
p_{T,τ_h}	12.4	0.14	0.12	0.02	0.01	0.2	0.14	0.12	0.03
m_T	11.0	0.12	0.11	0.01	0.008	0.18	0.12	0.11	0.02
$\not{E}_T$	11.0	0.12	0.11	0.01	0.008	0.18	0.12	0.11	0.02

Table 3: *Signal efficiency and background yields at the HL-LHC, in the* $pp \to H^\pm \to \tau_h\nu$ *channel, at each step of the cut-based analysis for the charged Higgs mass of* $m_{H^\pm} = 180$ *and* 400 *GeV.*

As previously mentioned, the $N_j \leq 2$ cut effectively reduces the $t\bar{t}$ background, resulting in a significant suppression. The $\Delta\phi(p_{T,\tau_h}, \not{p}_T)$ cut plays a crucial role in reducing all backgrounds while minimally affecting the signal process. For $m_{H^\pm} = 400$ GeV, the optimized cuts on p_{T,τ_h}, m_T, and $\not{E}_T$ lead to a reduction in all backgrounds by approximately one to two orders of magnitude. In Table 4, we provide the background yields and signal efficiencies after the cut-based analysis for $m_{H^\pm} = 200,\ 250,\ 300$, and 350 GeV. Indeed, for lower values of $m_{H^\pm} = 180$ GeV, the W+jets background contamination is significant, accounting for approximately 70% of the total background yield. The Misid. τ_h and DY+jets backgrounds contribute approximately 13% each. However, as $m_{H^\pm}$ increases, the signal and backgrounds become better separated, as evident from the kinematic distributions of p_{T,τ_h}, m_T, and $\not{E}_T$ in Fig. 3. This leads to a reduction in the W+jets background yield, and the contribution from Misid.τ_h becomes closer to the dominant W+jets background. For instance, after the cut-based analysis, the W+jets and Misid. τ_h backgrounds contribute approximately 47% and 42% to the total background yield, respectively, for $m_{H^\pm} = 400$ GeV.

To calculate the projected upper limit on the charged Higgs production cross-section in a model-independent way, we use the following formula:

$pp \to H^{\pm} \to \tau_h\nu$, $\sqrt{s} = 14$ TeV									
Masses	Background yields after the cut-based analysis at 3 ab^{-1}								Signal Efficiency,
$m_{H^{\pm}}$	W+jets	Misid. τ_h	DY+jets	$t\bar{t}$ had	$t\bar{t}$ semi-lep	$t\bar{t}$ lep	VV+jets	Single t	ϵ
(GeV)	($\times 10^7$)			($\times 10^5$)			($\times 10^6$)		($\times 10^{-2}$)
200	1.9	0.4	0.3	0.2	1.1	0.7	0.7	0.15	11.6
250	0.6	0.3	0.06	0.05	0.6	0.4	0.35	0.08	~ 10
300	0.36	0.2	0.04	0.03	0.4	0.3	0.25	0.06	10.9
350	0.2	0.16	0.02	0.02	0.3	0.2	0.16	0.04	10.9

Table 4: *Signal efficiency and background yields after the cut-based analysis in the $pp \to H^{\pm} \to \tau_h\nu$ channel at the HL-LHC.*

$$\sigma(pp \to H^{\pm} \to \tau_h\nu)_{\text{UL}} = \frac{N \cdot \sqrt{B}}{\epsilon \cdot \mathcal{L}} \tag{4.1}$$

where:

- $\sigma(pp \to H^{\pm} \to \tau_h\nu)_{\text{UL}}$ is the projected upper limit on the charged Higgs production cross-section in the $\tau_h\nu$ final state.
- N is the number of confidence intervals or the desired significance level. For example, a 95% confidence level corresponds to $N = 2$.
- B is the total background yield, which is the sum of all background events after the cut-based analysis.
- ϵ is the signal efficiency, representing the fraction of signal events that pass the selection cuts.
- $\mathcal{L}$ is the integrated luminosity, which denotes the total amount of data collected.

By plugging in the appropriate values for N, B, ϵ, and $\mathcal{L}$ from our analysis, we calculate the projected upper limit on the charged Higgs production cross-section. This provides an estimate of the maximum allowed cross-section for the charged Higgs production in the $\tau_h\nu$ final state based on the analysis results and the chosen confidence level.

We evaluate the $\sigma(pp \to H^{\pm} \to \tau_h\nu)_{\text{UL}}$ at different significance levels, such as 2σ (exclusion limit) and 5σ (discovery limit). The derived upper limits are shown as solid green and purple lines in Fig. 4. For example, for the 2σ upper limit, the values vary in the range [32.26 : 7.38] fb for $m_{H^{\pm}} = [180 : 400]$ GeV. These values represent the maximum allowed cross-section for the charged Higgs production in the $\tau_h\nu$ final state at a 95% confidence level. In addition, a systematic uncertainty of 2% is included in the analysis. The resulting upper

limits, accounting for this systematic uncertainty, are shown as dashed colored lines in Fig. 4. It is worth noting that the presence of systematics can weaken the limits due to the significant contamination from the W+jets background, which constitutes a substantial fraction of the total background (approximately $50 - 70\%$) in this channel.

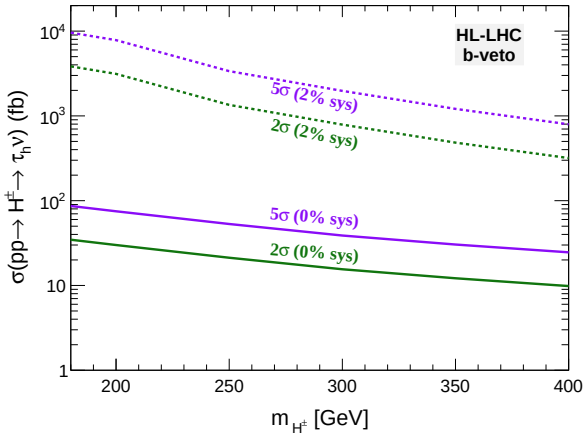

Figure 4: *Upper limit on $\sigma(pp \to H^{\pm} \to \tau\nu)$ as a function of $m_{H^{\pm}}$ in the b-veto category. The green and purple solid (dashed) lines show the 2σ and 5σ upper limit upon including* 0% (2%) *systematic uncertainties.*

4.2 The $b\tau_h\nu$ channel

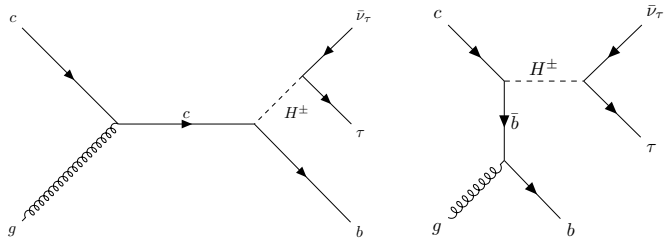

Figure 5: *The Feynman diagrams for the signal process $gc \to bH^{\pm} \to b\tau\nu$ in the b-tag category at leading order.*

In the $pp \to bH^{\pm} \to b\tau\nu$ channel, the charged Higgs boson is produced in association with a bottom quark. This final state is characterized by the presence of one b-tagged jet, along with the hadronically decaying tau lepton (τ_h) and missing transverse energy ($\not{E}_T$). The leading order Feynman diagrams for the signal process are shown in Fig. 5. We select events with exactly one τ-tagged jet with $p_T > 30$ GeV and $|\eta| < 4.0$. Leptons are vetoed having $p_T > 20$ GeV and $|\eta| < 4.0$. Events are required to have exactly one b-tagged jet with

$p_T > 30$ GeV and $|\eta| < 4.0$. We further restrict the total number of light jets to be at most two.

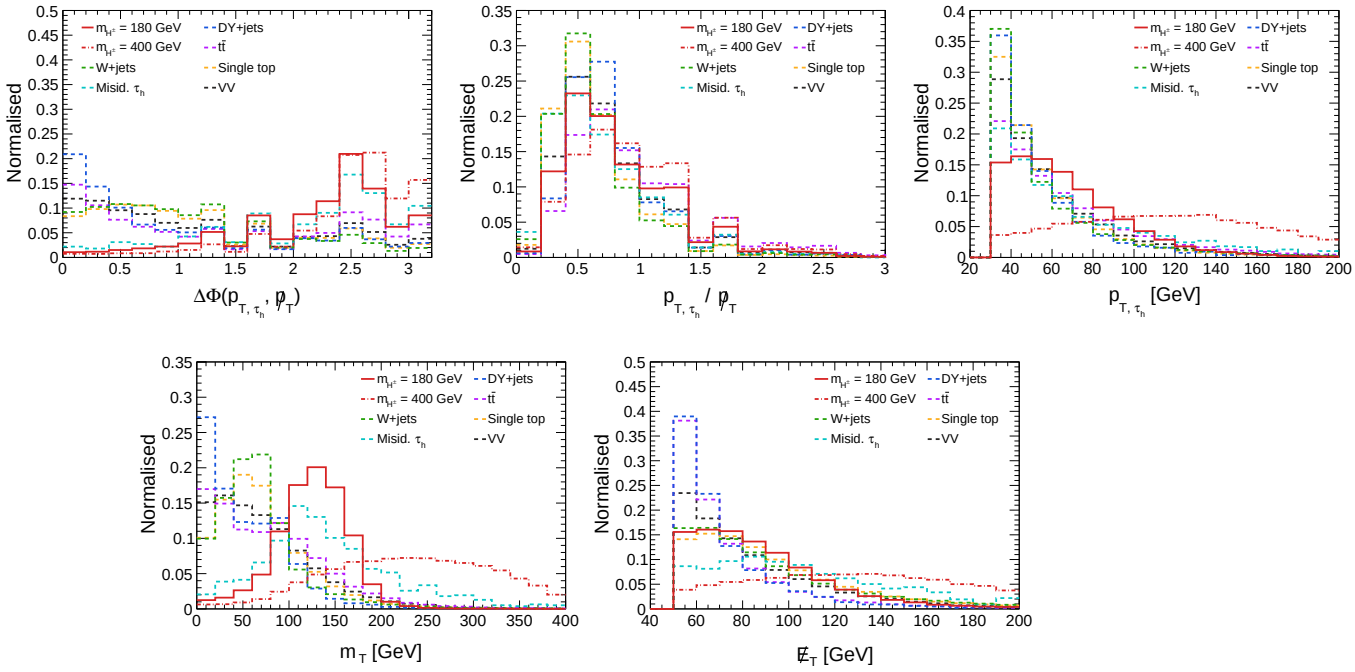

Figure 6: *The normalised kinematic distributions of $\Delta\phi(p_{T,\tau_h}, \not{p}_T)$, $p_{T,\tau_h}/\not{p}_T$, p_{T,τ_h}, m_T and $\not{E}_T$ for charged Higgs masses of $m_{H^\pm} = 180$ and 400 GeV with backgrounds, for the b-tag category. The distributions are shown after the basic trigger and generation level cuts.*

The normalised kinematic distributions of $\Delta\phi(p_{T,\tau_h}, \not{p}_T)$, $p_{T,\tau_h}/\not{p}_T$, p_{T,τ_h}, m_T, and $\not{E}_T$ for the $pp \to bH^\pm \to b\tau\nu$ channel are shown in Fig. 6. From the distributions, we observe that the signal and backgrounds overlap for the $p_{T,\tau_h}/\not{p}_T$ distribution. This can be understood by considering the additional b-jet present in the signal process. The charged Higgs recoils against the b-jet, which further decays to $\tau\nu$. The momentum imbalance of the b-jet and the hadronically decaying τ lepton contributes to the total missing transverse energy ($\not{E}_T$) in the event. As a result, the overall $\not{E}_T$ is higher compared to the previous b-veto signal category. The transverse momentum of the τ lepton is slightly lower in this final state. These factors lead to a decrease in the ratio $p_{T,\tau_h}/\not{p}_T$, causing the signal distribution to overlap with the background processes. Therefore, we exclude this observable from further optimization. Instead, we focus on four kinematic observables for the cut-based optimization: $\Delta\phi(p_{T,\tau_h}, \not{p}_T)$, p_{T,τ_h}, m_T, and $\not{E}_T$. These observables exhibit better discrimination between the signal and background processes. The trigger-level cuts and the optimized cuts for these observables are summarized in Table 5. These cuts are chosen to enhance the signal significance and improve

the sensitivity of the analysis.

Cuts applied	
Trigger cuts	
$N_{\tau_h} = 1,\ N_\ell = 0$ b-tag, $N_{\text{b-jets}} = 1$ $N_j \leq 2$	
Optimised cuts	
$p_{T,\tau_h} \geq [30, 30, 40, 50, 50, 60]$ GeV $\Delta\phi(p_{T,\tau_h}, \not{p}_T) \geq [1.1, 1.0, 0.9, 0.7, 1.0, 1.0]$ $m_T \geq [100, 110, 140, 170, 200, 230]$ GeV $\not{E}_T \geq [50, 50, 60, 70, 80, 100]$ GeV	for $m_{H^\pm} = [180, 200, 250, 300, 350, 400]$ GeV

Table 5: *Trigger-level and optimised cuts imposed on the cut-based analysis in b-tag category.*

The signal efficiency and background yields after each optimized cut for the $pp \to bH^\pm \to b\tau\nu$ channel at an integrated luminosity of 3 ab^{-1} are presented in Table 6. The most effective observable in reducing the backgrounds is the transverse mass, m_T. The cut on m_T becomes stronger as the charged Higgs mass increases, resulting in a reduction of the dominant W+jets background by approximately one order of magnitude. The $\Delta\phi(p_{T,\tau_h},\ \not{p}_T)$ variable is also effective in suppressing all background processes with a negligible impact on the signal efficiency. It helps to enhance the signal-to-background ratio by exploiting the back-to-back nature of the signal process, where the hadronically decaying τ and the missing transverse momentum are almost in opposite directions with dilution coming from the additional b-jet in this b-tag category. In Table 7, we provide the signal efficiency and background yields at a center-of-mass energy of $\sqrt{s} = 14$ TeV for charged Higgs mass, $m_{H^\pm} = 200,\ 250,\ 300$, and 350 GeV. These results demonstrate the effectiveness of the optimized cuts in enhancing the signal significance and reducing the background contributions.

Finally, we investigate the upper limits on the production cross-section, denoted as $\sigma(pp \to bH^\pm \to b\tau_h\nu)_{UL}$, in relation to the charged Higgs mass. The corresponding results are illustrated in Fig. 7. For the charged Higgs mass range of 180 GeV $\leq m_{H^\pm} \leq$ 400 GeV, the 95% confidence level (CL) upper limit, without any systematic uncertainties, exhibits a variation from 31.89 fb to 6.84 fb. When considering a 2% systematic uncertainty, the 2σ upper limit is approximately 70.26 fb for $m_{H^\pm} = 400$ GeV. Despite the additional b-tagging requirement favoring the $t\bar{t}$ background, this condition significantly suppresses the dominant W+jets background. Consequently, the upper limit in this channel becomes more stringent compared to the previously discussed $pp \to H^\pm \to \tau\nu$ final state due to a higher signal-to-background ratio (S/B).

Cut flow	Signal Efficiency, ϵ ($\times 10^{-2}$)	Background rates at $\sqrt{s} = 14$ TeV with $\mathcal{L} = 3$ ab^{-1}							
		W+jets	Misid. τ_h	DY+jets	$t\bar{t}$ had	$t\bar{t}$ semi-lep	$t\bar{t}$ lep	VV+jets	Single t
		($\times 10^6$)			($\times 10^5$)			($\times 10^6$)	
$m_{H^\pm} = 180$ GeV									
Trigger+Gen	7.0	4.8	0.6	1.8	18.3	83.5	15.6	8.0	5.2
$N_j \leq 2$	6.9	4.4	0.5	1.6	5.3	52.9	13.7	7.2	4.6
p_{T,τ_h}	6.9	4.4	0.5	1.6	5.3	52.9	13.7	7.2	4.6
$\Delta\phi(p_{T,\tau_h}, \not{p}_T)$	6.3	2.0	0.44	0.6	3.0	21.5	9.7	3.5	2.2
m_T	4.8	0.6	0.36	0.2	1.8	9.4	6.0	1.8	1.0
$\not{E}_T$	4.8	0.6	0.36	0.2	1.8	9.4	6.0	1.8	1.0
$m_{H^\pm} = 400$ GeV									
Trigger+Gen	13.0	4.8	0.6	1.8	18.3	83.5	15.6	8.0	5.2
$N_j \leq 2$	12.3	4.4	0.5	1.6	5.3	52.9	13.7	7.2	4.6
p_{T,τ_h}	10.8	1.3	0.3	0.5	2.7	18.0	4.5	2.6	1.5
$\Delta\phi(p_{T,\tau_h}, \not{p}_T)$	10.4	0.5	0.2	0.2	1.6	7.6	3.5	1.3	0.7
m_T	5.8	0.06	0.07	0.006	0.2	0.7	0.43	0.1	0.06
$\not{E}_T$	5.5	0.05	0.07	0.003	0.07	0.6	0.4	0.1	0.06

Table 6: *Signal efficiency and background yields at the HL-LHC, in the* $pp \to bH^\pm \to b\tau_h\nu$ *channel, at each step of the cut-based analysis for the charged Higgs mass of* $m_{H^\pm} = 180$ *and* 400 *GeV.*

$pp \to bH^\pm \to b\tau_h\nu$, $\sqrt{s} = 14$ TeV									
Masses $m_{H^\pm}$ (GeV)	Background yields after the cut-based analysis at 3 ab^{-1}								Signal Efficiency, ϵ ($\times 10^{-2}$)
	W+jets	Misid. τ_h	DY+jets	$t\bar{t}$ had	$t\bar{t}$ semi-lep	$t\bar{t}$ lep	VV+jets	Single t	
	($\times 10^6$)			($\times 10^5$)			($\times 10^6$)		
200	0.5	0.3	0.15	1.5	7.7	5.0	1.5	0.8	5.3
250	0.3	0.2	0.05	0.6	3.9	2.5	0.7	0.4	5.4
300	0.14	0.15	0.02	0.3	2.0	1.3	0.4	0.2	5.5
350	0.08	0.1	0.009	0.16	1.1	0.7	0.2	0.1	5.6

Table 7: *Signal efficiency and background yields after the cut-based analysis in the* $pp \to bH^\pm \to b\tau_h\nu$ *channel at the HL-LHC.*

5 Collider prospect of flavor anomalies

In the present section, we analyze the ramifications arising from the implementation of upper limits on the cross-section of charged Higgs production, focusing on their impact on the Yukawa parameter space as well as the extent to which the HL-LHC can effectively probe the diverse anomalies observed in the $b \to c\tau\nu$ decay processes.

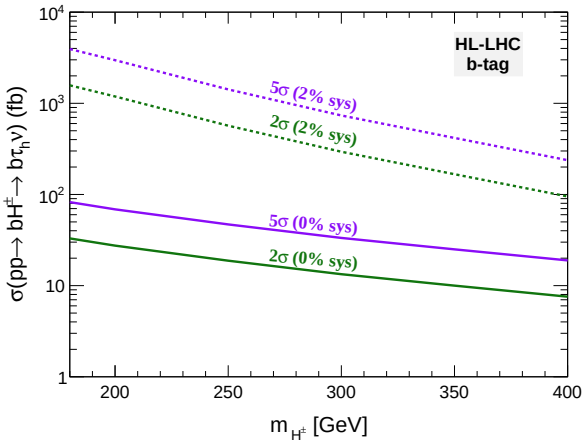

Figure 7: *Upper limit on $\sigma(pp \to H^{\pm} \to \tau\nu)$ as a function of charged Higgs mass in the b-tag category. The green and purple solid (dashed) lines show the 2σ and 5σ upper limit upon including* 0% (2%) *systematic uncertainties.*

5.1 The Yukawa coupling plane

From Eq. 3.3, it is evident that the scalar coupling C^S_{RR} is directly proportional to the product of the charged Higgs Yukawa couplings, $\tilde{y}_{bc} \times \tilde{y}_{\tau\nu}$. The objective of this section is to scrutinize the two-dimensional parameter space of Yukawa couplings, namely $|\tilde{y}_{bc}| - |\tilde{y}_{\tau\nu}|$. For our analysis, we consider the charged Higgs mass to lie within the range of [180, 400] GeV. In Fig. 8, we show the 1σ and 2σ allowed region of Yukawa couplings $|\tilde{y}_{bc}|$ and $|\tilde{y}_{\tau\nu}|$ favored by R_D, $R_{D^\star}$, $P^{D^\star}_\tau$, $F^{D^\star}_L$, $R_{J/\psi}$, and R_{Λ_c}, represented by the darker and light yellow band, respectively. These allowed regions are obtained by minimizing χ^2 of a negative log-likelihood function. The bands demonstrate consistency of the Yukawa coupling product, $\tilde{y}_{bc} \times \tilde{y}_{\tau\nu}$, with current measurements of all the considered flavor observables. It is evident that the $|\tilde{y}_{bc}| - |\tilde{y}_{\tau\nu}|$ parameter space is more constrained for low mass charged Higgs boson. Additionally, the region below the solid blue line corresponds to the allowed parameter space considering a $\mathcal{B}(B_c \to \tau\nu)$ branching ratio of 63%. Further, the large $\tilde{y}_{bc}$ values are subject to constraints from $B_s - \bar{B}_s$ mixing, as illustrated by the excluded gray colored region in the figure. We account for the renormalization group equation (RGE) running effect of the strong coupling constant α_s [65]. The contribution of the charged Higgs to the $B_s - \bar{B}_s$ mixing, occurring at the 1-loop level, is taken from [26], and we follow [66] to impose constraint on this parameter. The constraint is stronger (larger gray colored region) for low mass charged Higgs boson and it reduces the allowed $|\tilde{y}_{bc}| - |\tilde{y}_{\tau\nu}|$ parameter space significantly. Finally, we incorporate the 95% confidence level (CL) upper limits obtained from the $\tau_h\nu$ (b-veto category) and $b\tau_h\nu$ (b-tag category) searches discussed in the previous section. These upper

limits are represented by the green and purple colored lines, respectively, in Fig. 8. The collider search, specifically b-tag analysis can probe the remaining region of parameter space in $|\tilde{y}_{bc}| - |\tilde{y}_{\tau\nu}|$ plane for higher charged Higgs masses.

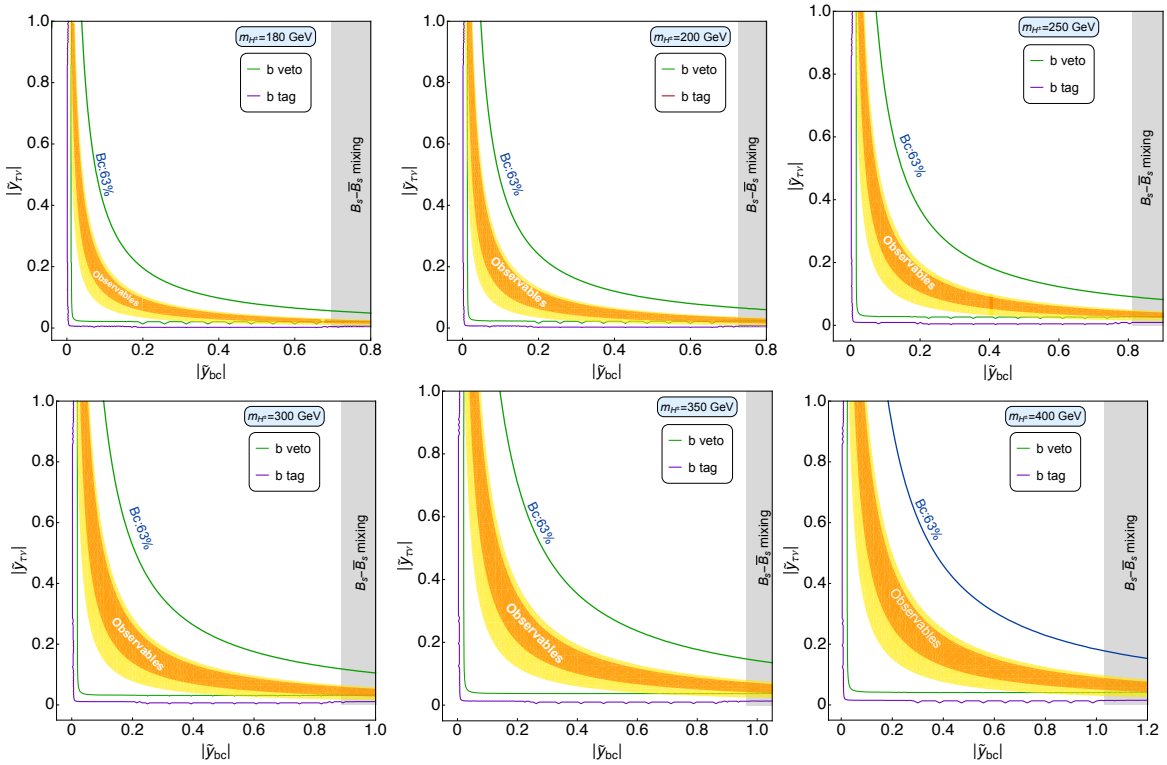

Figure 8: *Constraints on $|\tilde{y}_{bc}| - |\tilde{y}_{\tau\nu}|$ parameter space for various charged Higgs masses. The darker yellow and light yellow bands indicate the 1σ and 2σ region in consonant with the current measurement of corresponding flavor observables. Here, Bc represents the $\mathcal{B}(B_c \to \tau\nu)$. The collider constraints are shown with green and purple lines for b-veto and b-tag analysis, respectively.*

5.2 Accessible region in the flavor observable planes

In Figure 9, we illustrate the flavor observables in several 2D planes, similar to Fig. 1. The black star denotes the SM prediction. The experimental central value is represented by the blue star and the corresponding 1σ and 2σ uncertainty is represented with solid and dashed blue contour, respectively. The best fit value of C_{RR}^S coupling is denoted with a red circle. Next, we evaluate the accessible region in these flavor observable planes in case of charged Higgs coupled to a right-handed neutrino in G2HDM model and it is shown with the solid green line. The points on the green line are the only accessible values within the current model, which passes through the SM and the best fit value of C_{RR}^S coupling. The line is

evaluated by solving for Yukawa couplings after inserting C_{RR}^S of Eq. 3.3 into Eq. 2.2. For large $\tilde{y}_{bc}$ values, the constraint from b-veto category almost falls within the 2σ contour of flavor observables (see Fig. 8). Therefore, we select two benchmark points for b-tag category based on the collider constraints obtained in the $|\tilde{y}_{bc}|-|\tilde{y}_{\tau\nu}|$ plane. Specifically, we consider the points $(|\tilde{y}_{bc}|, |\tilde{y}_{\tau\nu}|) \sim (0.6, 0.022)$ and $(0.9, 0.016)$ for $m_{H^\pm} = 180$ and 400 GeV, respectively. These constraints are then translated into the 2D plane of flavor observables, as shown in Figure 9. In the figure, we represent the benchmark points for the 180 and 400 GeV with purple and yellow-colored tick symbol, respectively. A significant part of the green line and the HL-LHC accessible points lie within the 2σ contour. To summarize, current measurement of flavor observables is within the reach of the considered model at 2σ uncertainty.

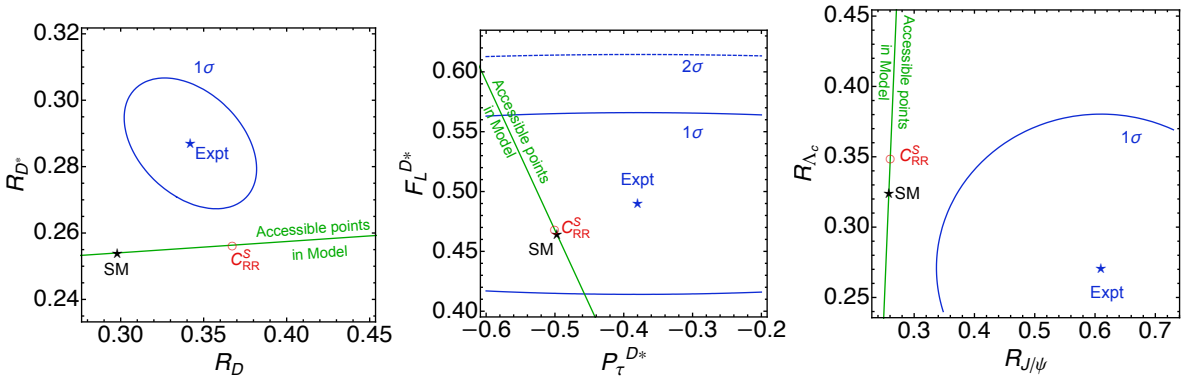

Figure 9: *Accessible region in the flavor observable planes. The points on the green colored line are accessible in the present model.*

6 Summary and outlook

Experimental measurements of various flavor ratios, such as R_D, $R_{D^\star}$, $P_\tau^{D^\star}$, $F_L^{D^\star}$, $R_{J/\psi}$, and R_{Λ_c} exhibit deviations from SM. If these deviations persist in future experiments, it would provide unequivocal evidence of physics beyond the SM.

In this study, we explore these anomalies by considering an effective Lagrangian that incorporates new physics coming from right handed neutrinos. In order to determine the NP coupling, we perform a χ^2 fit by including six measurements, namely R_D, $R_{D^\star}$, $P_\tau^{D^\star}$, $F_L^{D^\star}$, $R_{J/\psi}$ and R_{Λ_c}. We obtain the best fit value to be $C_{RR}^S/C_{LR}^S = -0.51$. We analyzed the impact of the NP scalar couplings on $R_D - R_{D^\star}$, $P_\tau^{D^\star} - F_L^{D^\star}$ and $R_{J/\psi} - R_{\Lambda_c}$. From the R_D-$R_{D^\star}$ plane, we observe that although the best-fit value lies within the 2σ contour, the 1σ region around the best fit value overlaps with the 1σ experimental contour. Further, we observe that the range of $\mathcal{B}(B_c \to \tau\nu)$ obtained with C_{RR}^S/C_{LR}^S NP coupling satisfy the $\mathcal{B}(B_c \to \tau\nu) \leq 63\%$ constraint.

We further study the flavor anomalies in case of charged Higgs coupled to a right-handed neutrino in the context of G2HDM model. We perform a collider study with charged Higgs boson in order to explain the $b \to c\tau\nu$ anomalies in presence of right-handed scalar coupling, in the following two final states: $pp \to H^{\pm} \to \tau\nu$ and $pp \to bH^{\pm} \to b\tau\nu$, at a center of mass energy of $\sqrt{s} = 14$ TeV, with an integrated luminosity of 3 ab^{-1}. Our study involves a comprehensive collider analysis, wherein we optimize the selection cuts on various kinematic observables for a set of benchmark masses for the charged Higgs boson, specifically $m_{H^{\pm}} = [180, 200, 250, 300, 350, 400]$ GeV. The $pp \to bH^{\pm} \to b\tau\nu$ final state, also referred to as the b-tag category, exhibits lower contamination from the dominant W+jets background. Consequently, the addition of systematic uncertainties has a lesser impact on this channel. This advantage can be attributed to the additional requirement of b-tagging in the $b\tau\nu$ final state, which aids in reducing background contributions. Next, we show that the allowed Yukawa plane, $|\tilde{y}_{bc}| - |\tilde{y}_{\tau\nu}|$, is heavily constrained with recent experimental measurements. The upper limits obtained for $\sigma(pp \to bH^{\pm} \to b\tau\nu)$ impose a more stringent constraint on the Yukawa plane compared to the upper limits on $\sigma(pp \to H^{\pm} \to \tau\nu)$ from b-veto category. Additionally, we explore the accessible regions for the model in these flavor observable planes. From our analysis, we observe that the accessible values of the flavor observables in G2HDM model lie within the 2σ region of the experimental measurement. Further, HL-LHC has the potential to exclude these currently allowed regions.

Acknowledgments

We would like to thank N. Rajeev, Girish Kumar, Syuhei Iguro, Biplob Bhattacherjee and Ayan Paul for helpful discussions throughout the course of this work. We would also like to thank Wolfgang Altmannshofer for the fruitful discussion on the topics addressed in this article. A.A. thanks the Planck conference, University of Warsaw for hospitality where discussions and part of this work was completed. AA received support from the French government under the France 2030 investment plan, as part of the Initiative d'Excellence d'Aix-Marseille Université - A*MIDEX.

A Detail of the generation cuts and production cross section of backgrounds

Process	Backgrounds	Generation-level cuts ($\ell = e^{\pm}, \mu^{\pm}, \tau^{\pm}$) (NA : Not Applied)	Cross section (fb)
$\tau_h\nu$ / $b\tau_h\nu$	$t\bar{t}$ hadronic[1]	$p_{T,j/b} > 20$ GeV, $p_{T,\ell} > 15$ GeV, $\lvert\eta_{j/b/\ell}\rvert < 5.0$, $\Delta R_{j,b,\ell} > 0.2$, $\not{E}_T > 50$ GeV	199840.6
	$t\bar{t}$ semi-leptonic	same as $t\bar{t}$ hadronic	41051.6
	$t\bar{t}$ leptonic		5483.4
	W + jets		672182
	Misid. τ_h		497287
	DY + jets		1584131.4
	ZZ + jets		12276.8
	WZ + jets		41286.5
	WW + jets		360887
	Single top Wt-channel		26489.8

Table 8: *The generation level cuts for various backgrounds used in the analyses along with the production cross-sections.*

B Detail of the input parameters

Parameters	Values	Parameters	Values
m_{B^-}	5.27931	m_{B_c}	6.2751
$m_{J/\Psi}$	3.0969	$m_{D^{*0}}$	2.00685
m_{Λ_b}	5.61951	m_{Λ_c}	2.28646
τ_{B_c}	0.507×10^{-12}	f_{B_c}	0.434(0.015)
τ_{B^-}	1.638×10^{-12}	$m_{D^{*0}}$	2.00685
τ_{Λ_b}	$(1.466 \pm 0.010) \times 10^{-12}$		
m_{B_c}	6.272	$m_{B_c^\star}$	6.332
m_e	$0.5109989461 \times 10^{-3}$	m_τ	1.77682
m_b	4.18	m_c	0.91
V_{cb}	0.0409(11)	G_F	1.1663787×10^{-5}

Table 9: *Input parameters [68]. Masses are quoted in units of GeV and lifetimes are shown in units of second, at the renormalization scale $\mu = m_b$.*

[1]The $t\bar{t}$ production cross-sections are taken at NNLO order [67].

References

[1] BaBar collaboration, J. P. Lees et al., *Evidence for an excess of $\bar{B} \to D^{(*)}\tau^-\bar{\nu}_\tau$ decays*, *Phys. Rev. Lett.* **109** (2012) 101802, [1205.5442].

[2] BaBar collaboration, J. P. Lees et al., *Measurement of an Excess of $\bar{B} \to D^{(*)}\tau^-\bar{\nu}_\tau$ Decays and Implications for Charged Higgs Bosons*, *Phys. Rev. D* **88** (2013) 072012, [1303.0571].

[3] Belle collaboration, M. Huschle et al., *Measurement of the branching ratio of $\bar{B} \to D^{(*)}\tau^-\bar{\nu}_\tau$ relative to $\bar{B} \to D^{(*)}\ell^-\bar{\nu}_\ell$ decays with hadronic tagging at Belle*, *Phys. Rev. D* **92** (2015) 072014, [1507.03233].

[4] Belle collaboration, Y. Sato et al., *Measurement of the branching ratio of $\bar{B}^0 \to D^{*+}\tau^-\bar{\nu}_\tau$ relative to $\bar{B}^0 \to D^{*+}\ell^-\bar{\nu}_\ell$ decays with a semileptonic tagging method*, *Phys. Rev. D* **94** (2016) 072007, [1607.07923].

[5] Belle collaboration, G. Caria et al., *Measurement of $\mathcal{R}(D)$ and $\mathcal{R}(D^*)$ with a semileptonic tagging method*, *Phys. Rev. Lett.* **124** (2020) 161803, [1910.05864].

[6] LHCb collaboration, R. Aaij et al., *Measurement of the ratio of branching fractions $\mathcal{B}(\bar{B}^0 \to D^{*+}\tau^-\bar{\nu}_\tau)/\mathcal{B}(\bar{B}^0 \to D^{*+}\mu^-\bar{\nu}_\mu)$*, *Phys. Rev. Lett.* **115** (2015) 111803, [1506.08614].

[7] LHCb collaboration, R. Aaij et al., *Measurement of the ratio of the $B^0 \to D^{*-}\tau^+\nu_\tau$ and $B^0 \to D^{*-}\mu^+\nu_\mu$ branching fractions using three-prong τ-lepton decays*, *Phys. Rev. Lett.* **120** (2018) 171802, [1708.08856].

[8] LHCb collaboration, R. Aaij et al., *Test of Lepton Flavor Universality by the measurement of the $B^0 \to D^{*-}\tau^+\nu_\tau$ branching fraction using three-prong τ decays*, *Phys. Rev. D* **97** (2018) 072013, [1711.02505].

[9] LHCb collaboration, *"First joint measurement of $R(D^*)$ and $R(D^0)$ at LHCb."* *https://indico.cern.ch/event/1187939/*, .

[10] https://hflav-eos.web.cern.ch/hflav-eos/semi/winter23_prel/html/RDsDsstar/RDRDs.html.

[11] LHCb collaboration, R. Aaij et al., *Measurement of the ratio of branching fractions $\mathcal{B}(B_c^+ \to J/\psi\tau^+\nu_\tau)/\mathcal{B}(B_c^+ \to J/\psi\mu^+\nu_\mu)$*, *Phys. Rev. Lett.* **120** (2018) 121801, [1711.05623].

[12] S. Iguro, T. Kitahara and R. Watanabe, *Global fit to $b \to c\tau\nu$ anomalies as of Spring 2024*, *Phys. Rev. D* **110** (2024) 075005, [2405.06062].

[13] LHCb collaboration, R. Aaij et al., *Observation of the decay $\Lambda_b^0 \to \Lambda_c^+\tau^-\bar{\nu}_\tau$*, *Phys. Rev. Lett.* **128** (2022) 191803, [2201.03497].

[14] Belle collaboration, S. Hirose et al., *Measurement of the τ lepton polarization and $R(D^*)$ in the decay $\bar{B} \to D^*\tau^-\bar{\nu}_\tau$*, *Phys. Rev. Lett.* **118** (2017) 211801, [1612.00529].

[15] Belle collaboration, S. Hirose et al., *Measurement of the τ lepton polarization and $R(D^*)$ in the decay $\bar{B} \to D^*\tau^-\bar{\nu}_\tau$ with one-prong hadronic τ decays at Belle*, *Phys. Rev. D* **97** (2018) 012004, [1709.00129].

[16] Belle collaboration, A. Abdesselam et al., *Measurement of the D^{*-} polarization in the decay $B^0 \to D^{*-}\tau^+\nu_\tau$*, in *10th International Workshop on the CKM Unitarity Triangle*, 3, 2019. 1903.03102.

[17] A. Crivellin, C. Greub and A. Kokulu, *Explaining $B \to D\tau\nu$, $B \to D^*\tau\nu$ and $B \to \tau\nu$ in a 2HDM of type III*, *Phys. Rev. D* **86** (2012) 054014, [1206.2634].

[18] A. Celis, M. Jung, X.-Q. Li and A. Pich, *Sensitivity to charged scalars in $\boldsymbol{B \to D^{(*)}\tau\nu_\tau}$ and $\boldsymbol{B \to \tau\nu_\tau}$ decays*, *JHEP* **01** (2013) 054, [1210.8443].

[19] M. Tanaka and R. Watanabe, *New physics in the weak interaction of $\bar{B} \to D^{(*)}\tau\bar{\nu}$*, *Phys. Rev. D* **87** (2013) 034028, [1212.1878].

[20] P. Ko, Y. Omura and C. Yu, *$B \to D^{(}*)\tau\nu$ and $B \to \tau\nu$ in chiral $U(1)'$ models with flavored multi Higgs doublets*, *JHEP* **03** (2013) 151, [1212.4607].

[21] A. Crivellin, A. Kokulu and C. Greub, *Flavor-phenomenology of two-Higgs-doublet models with generic Yukawa structure*, *Phys. Rev. D* **87** (2013) 094031, [1303.5877].

[22] A. Crivellin, J. Heeck and P. Stoffer, *A perturbed lepton-specific two-Higgs-doublet model facing experimental hints for physics beyond the Standard Model*, *Phys. Rev. Lett.* **116** (2016) 081801, [1507.07567].

[23] C. S. Kim, Y. W. Yoon and X.-B. Yuan, *Exploring top quark FCNC within 2HDM type III in association with flavor physics*, *JHEP* **12** (2015) 038, [1509.00491].

[24] J. M. Cline, *Scalar doublet models confront τ and b anomalies*, *Phys. Rev. D* **93** (2016) 075017, [1512.02210].

[25] J.-P. Lee, *$B \to D^{(*)}\tau\nu_\tau$ in the 2HDM with an anomalous τ coupling*, *Phys. Rev. D* **96** (2017) 055005, [1705.02465].

[26] S. Iguro and K. Tobe, *$R(D^{(*)})$ in a general two Higgs doublet model*, *Nucl. Phys. B* **925** (2017) 560–606, [1708.06176].

[27] S. Iguro, Y. Omura and M. Takeuchi, *Test of the $R(D^{(*)})$ anomaly at the LHC*, *Phys. Rev. D* **99** (2019) 075013, [1810.05843].

[28] S. Iguro and Y. Omura, *Status of the semileptonic B decays and muon g-2 in general 2HDMs with right-handed neutrinos*, *JHEP* **05** (2018) 173, [1802.01732].

[29] C.-H. Chen and T. Nomura, *Charged Higgs boson contribution to $B_q^- \to \ell\bar{\nu}$ and $\bar{B} \to (P,V)\ell\bar{\nu}$ in a generic two-Higgs doublet model*, *Phys. Rev. D* **98** (2018) 095007, [1803.00171].

[30] R. Martinez, C. F. Sierra and G. Valencia, *Beyond $\mathcal{R}(D^{(*)})$ with the general type-III 2HDM for $b \to c\tau\nu$*, *Phys. Rev. D* **98** (2018) 115012, [1805.04098].

[31] D. J. Robinson, B. Shakya and J. Zupan, *Right-handed neutrinos and $R(D^{()})$*, *JHEP* **02** (2019) 119, [1807.04753].

[32] S.-P. Li, X.-Q. Li, Y.-D. Yang and X. Zhang, *$R_{D^{(*)}}, R_{K^{(*)}}$ and neutrino mass in the 2HDM-III with right-handed neutrinos*, *JHEP* **09** (2018) 149, [1807.08530].

[33] J. Cardozo, J. H. Muñoz, N. Quintero and E. Rojas, *Analysing the charged scalar boson contribution to the charged-current B meson anomalies*, *J. Phys. G* **48** (2021) 035001, [2006.07751].

[34] P. Athron, C. Balazs, T. E. Gonzalo, D. Jacob, F. Mahmoudi and C. Sierra, *Likelihood analysis of the flavour anomalies and g – 2 in the general two Higgs doublet model*, *JHEP* **01** (2022) 037, [2111.10464].

[35] S. Iguro, *Revival of H- interpretation of RD(*) anomaly and closing low mass window*, *Phys. Rev. D* **105** (2022) 095011, [2201.06565].

[36] M. Blanke, S. Iguro and H. Zhang, *Towards ruling out the charged Higgs interpretation of the $R_{D^{(*)}}$ anomaly*, *JHEP* **06** (2022) 043, [2202.10468].

[37] G. Kumar, *Interplay of the charged Higgs boson effects in $R_{D^{(*)}}$, $b \to s\ell^+\ell^-$, and W mass*, *Phys. Rev. D* **107** (2023) 075016, [2212.07233].

[38] S. Iguro, *Conclusive probe of the charged Higgs solution of P5' and RD(*) discrepancies*, *Phys. Rev. D* **107** (2023) 095004, [2302.08935].

[39] J. Aebischer and B. Grinstein, *Standard Model prediction of the B_c lifetime*, *JHEP* **07** (2021) 130, [2105.02988].

[40] T. P. Cheng and M. Sher, *Mass-matrix ansatz and flavor nonconservation in models with multiple higgs doublets*, *Phys. Rev. D* **35** (Jun, 1987) 3484–3491.

[41] G. C. Branco, P. M. Ferreira, L. Lavoura, M. N. Rebelo, M. Sher and J. P. Silva, *Theory and phenomenology of two-Higgs-doublet models*, *Phys. Rept.* **516** (2012) 1–102, [1106.0034].

[42] T. Bhattacharya, V. Cirigliano, S. D. Cohen, A. Filipuzzi, M. Gonzalez-Alonso, M. L. Graesser et al., *Probing Novel Scalar and Tensor Interactions from (Ultra)Cold Neutrons to the LHC*, *Phys. Rev. D* **85** (2012) 054512, [1110.6448].

[43] V. Cirigliano, J. Jenkins and M. Gonzalez-Alonso, *Semileptonic decays of light quarks beyond the Standard Model*, *Nucl. Phys. B* **830** (2010) 95–115, [0908.1754].

[44] S. Iguro, T. Kitahara and R. Watanabe, *Global fit to $b \to c\tau\nu$ anomalies 2022 mid-autumn*, 2210.10751.

[45] R. Mandal, C. Murgui, A. Peñuelas and A. Pich, *The role of right-handed neutrinos in $b \to c\tau\bar{\nu}$ anomalies*, *JHEP* **08** (2020) 022, [2004.06726].

[46] S. Iguro and R. Watanabe, *Bayesian fit analysis to full distribution data of $\overline{\mathrm{B}} \to \mathrm{D}^{(*)}\ell\overline{\nu}$: $|\mathrm{V_{cb}}|$ determination and new physics constraints*, *JHEP* **08** (2020) 006, [2004.10208].

[47] M. Blanke, A. Crivellin, S. de Boer, T. Kitahara, M. Moscati, U. Nierste et al., *Impact of polarization observables and $B_c \to \tau\nu$ on new physics explanations of the $b \to c\tau\nu$ anomaly*, *Phys. Rev. D* **99** (2019) 075006, [1811.09603].

[48] MILC collaboration, J. A. Bailey et al., *$B \to D\ell\nu$ form factors at nonzero recoil and $-V_{cb}-$ from 2+1-flavor lattice QCD*, *Phys. Rev. D* **92** (2015) 034506, [1503.07237].

[49] HPQCD collaboration, J. Harrison, C. T. H. Davies and A. Lytle, *$B_c \to J/\psi$ form factors for the full q^2 range from lattice QCD*, *Phys. Rev. D* **102** (2020) 094518, [2007.06957].

[50] W. Detmold, C. Lehner and S. Meinel, *$\Lambda_b \to p\ell^-\bar{\nu}_\ell$ and $\Lambda_b \to \Lambda_c\ell^-\bar{\nu}_\ell$ form factors from lattice QCD with relativistic heavy quarks*, *Phys. Rev. D* **92** (2015) 034503, [1503.01421].

[51] I. Caprini, L. Lellouch and M. Neubert, *Dispersive bounds on the shape of anti-B —> D(*) lepton anti-neutrino form-factors*, *Nucl. Phys. B* **530** (1998) 153–181, [hep-ph/9712417].

[52] F. James and M. Roos, *Minuit - a system for function minimization and analysis of the parameter errors and correlations*, *Computer Physics Communications* **10** (1975) 343–367.

[53] H. Dembinski, P. Ongmongkolkul, C. Deil, H. Schreiner, M. Feickert, Andrew et al., *scikit-hep/iminuit: v*, Feb., 2023. 10.5281/zenodo.7630430.

[54] M. Freytsis, Z. Ligeti and J. T. Ruderman, *Flavor models for $\bar{B} \to D^{(*)}\tau\bar{\nu}$*, *Phys. Rev. D* **92** (2015) 054018, [1506.08896].

[55] CMS collaboration, *Search for new physics in the τ lepton plus missing transverse momentum final state in proton-proton collisions at $\sqrt{s}$ = 13 TeV*, 2212.12604.

[56] CMS collaboration, A. M. Sirunyan et al., *Search for a W' boson decaying to a τ lepton and a neutrino in proton-proton collisions at $\sqrt{s}$ = 13 TeV*, *Phys. Lett. B* **792** (2019) 107–131, [1807.11421].

[57] J. Alwall, R. Frederix, S. Frixione, V. Hirschi, F. Maltoni, O. Mattelaer et al., *The automated computation of tree-level and next-to-leading order differential cross sections, and their matching to parton shower simulations*, *JHEP* **07** (2014) 079, [1405.0301].

[58] NNPDF collaboration, R. D. Ball et al., *Parton distributions for the LHC Run II*, *JHEP* **04** (2015) 040, [1410.8849].

[59] T. Sjöstrand, S. Ask, J. R. Christiansen, R. Corke, N. Desai, P. Ilten et al., *An introduction to PYTHIA 8.2*, *Comput. Phys. Commun.* **191** (2015) 159–177, [1410.3012].

[60] *ATLAS Run 1 Pythia8 tunes*, Tech. Rep. ATL-PHYS-PUB-2014-021, CERN, Geneva, Nov, 2014.

[61] M. Cacciari, G. P. Salam and G. Soyez, *FastJet User Manual*, *Eur. Phys. J.* **C72** (2012) 1896, [1111.6097].

[62] M. Cacciari, G. P. Salam and G. Soyez, *The Anti-k(t) jet clustering algorithm*, *JHEP* **04** (2008) 063, [0802.1189].

[63] DELPHES 3 collaboration, J. de Favereau, C. Delaere, P. Demin, A. Giammanco, V. Lemaître, A. Mertens et al., *DELPHES 3, A modular framework for fast simulation of a generic collider experiment*, *JHEP* **02** (2014) 057, [1307.6346].

[64] M. L. Mangano, M. Moretti, F. Piccinini and M. Treccani, *Matching matrix elements and shower evolution for top-quark production in hadronic collisions*, *JHEP* **01** (2007) 013, [hep-ph/0611129].

[65] D. Marzocca, U. Min and M. Son, *Bottom-Flavored Mono-Tau Tails at the LHC*, *JHEP* **12** (2020) 035, [2008.07541].

[66] L. Di Luzio, M. Kirk, A. Lenz and T. Rauh, ΔM_s *theory precision confronts flavour anomalies*, *JHEP* **12** (2019) 009, [1909.11087].

[67] https://twiki.cern.ch/twiki/bin/view/LHCPhysics/TtbarNNLO.

[68] Particle Data Group collaboration, R. L. Workman et al., *Review of Particle Physics*, *PTEP* **2022** (2022) 083C01.